Monthly Notices
of the
ROYAL ASTRONOMICAL SOCIETY

Mon. Not. R. Astron. Soc. **423,** 493–504 (2012) doi:10.1111/j.1365-2966.2012.20894.x

# *Chandra* study of the eclipsing M dwarf binary, YY Gem

G. A. J. Hussain,[1⋆] N. S. Brickhouse,[2] A. K. Dupree,[2] F. Reale,[3] F. Favata[4] and M. M. Jardine[5]

[1]*ESO, Karl-Schwarzschild-Strasse 2, 85748 Garching, Germany*
[2]*Harvard–Smithsonian Center for Astrophysics, 60 Garden Street, Cambridge, MA 02138, USA*
[3]*Dipartimento di Fisica, Università degli Studi di Palermo, Piazza del Parlamento 1, 90134 Palermo, Italy*
[4]*European Space Agency, 8-10 rue Mario Nikis, 75015 Paris, France*
[5]*School of Physics and Astronomy, University of St Andrews, St Andrews, Fife KY16 9SS*

Accepted 2012 March 8. Received 2012 March 7; in original form 2011 December 4

## ABSTRACT

The eclipsing M dwarf binary system, YY Gem, was observed using *Chandra* covering 140 ks ($2P_{\rm rot}$) in total, split into two even exposures separated by 0.76 d ($0.94\,P_{\rm rot}$). The system was extremely active: three energetic flares were observed over the course of these observations. The flaring and non-flaring states of the system are analysed in this paper. The activity level increased between the first and second observations even during the quiescent (non-flaring) phases. An analysis of the dynamics of the X-ray-emitting plasma suggests that both components are significantly active. Contemporaneous H$\alpha$ spectra also suggest that both components show similar levels of activity.

The primary star is the likely source of at least two of the flares. From a detailed analysis of the flare emission at the maximum temperature and maximum density with single loop flare models, we find loop lengths of $\sim$0.7$R_*$, 1.5$R_*$ and 1.8$R_*$. All of these flares are strongly associated with hot (>10 MK) X-ray emission which appears to predominantly trace the orbital motion of the primary star. The two largest flaring loops are similar to the largest sizes reported in other active M stars and span nearly half the interbinary system; this may indicate magnetospheric interaction between the binary star coronae. We discuss the time and spectral resolution requirements that are necessary to recover detailed information about coronal structure from the X-ray spectra in similar cool star systems.

**Key words:** techniques: spectroscopic – binaries: eclipsing – stars: coronae – stars: flare – stars: magnetic field – X-rays: stars.

## 1 INTRODUCTION

Time-resolved X-ray spectroscopy can provide insights into the sizes and structure of both non-flaring and flaring X-ray-emitting coronae in cool stars (Favata et al. 2000; Sanz-Forcada, Brickhouse & Dupree 2003). With the availability of the higher spectroscopic resolution capabilities in the *Chandra* and *XMM–Newton* satellites, we can trace dynamic information in cool star systems in greater detail than previously possible.

Dynamic studies of W UMa type contact binary systems at X-ray wavelengths have yielded important advances in probing the quiescent structure of cool star coronae. As these systems have short orbital periods, it is possible to cover several rotation periods in a relatively short time, and thus disentangle flaring and stable quiescent X-ray emission. Brickhouse, Dupree & Young (2001) observed 44i Boo (G0V+G0V, $P_{\rm rot}$ = 0.27 d) over 2.5 $P_{\rm rot}$ using *Chandra* High Energy Transmission Grating (HETG; Canizares et al. 2005). From the rotational modulation observed in the system's X-ray light curves and the Doppler shifts in its X-ray line profiles, they deduce that the emission from the system is dominated by compact emission at high latitudes. Observations of the contact binary, VW Cep (K0V+G5V, $P_{\rm rot}$ = 0.28 d), covering 4.8 $P_{\rm rot}$ also show evidence for a high-latitude, compact X-ray corona, predominantly concentrated on the primary star (Huenemoerder, Testa & Buzasi 2006).

A multiwavelength study of the single rapidly rotating star AB Dor (K0V, $P_{\rm rot}$ = 0.51 d) reveals evidence of rotational modulation in both the X-ray light curves and spectra (Hussain et al. 2007). The authors find that its corona must be compact, based on the coronal densities measured in its O VII diagnostic along with complex magnetic field distribution found via contemporaneous surface magnetic field maps (obtained with ground-based spectropolarimetry). Furthermore, a significant high-latitude component is required to explain the relatively low rotational modulation observed on the system.

⋆E-mail: ghussain@eso.org

We observe the eclipsing binary, YY Gem (M1V+M1V, $P_{\rm rot}$ = 0.81d), using *Chandra*/HETG observations in conjunction with optical spectroscopy. We aim to study the structure of the stellar coronae by following the system over $2P_{\rm rot}$. To study the dynamics in the system, we build composite line profiles from the strongest emission-line profiles in the X-ray data. The observations are described in Section 2; the X-ray light curves and spectra are presented in Sections 3 and 4, respectively. An analysis of the dynamics of the non-flaring and flaring coronae of the M star components of YY Gem is presented in Section 5. In Section 6, we analyse the flares observed in our X-ray observations using the techniques developed by Reale (2007).

### 1.1 YY Gem

YY Gem (Castor C, BD+32 1582, HD 60179 C, Gliese 278 C) is an eclipsing binary system that is strongly magnetically active, as evidenced by (i) YY Gem's high flaring rate, (ii) dark cool starspots from photometry and spectroscopy and (iii) X-ray variability (Kron 1952; Golub, Harnden & Maxson 1983; Doyle & Butler 1985; Hatzes 1995; Butler, Doyle & Budding 1996; Güdel et al. 2001; Stelzer et al. 2002). YY Gem is part of the Castor sextuplet, located 71 arcsec south of Castor A and B. Castor A and B are also spectroscopic binaries (albeit single lined) and have an angular separation from each other of about 3.9 arcsec. YY Gem is an eclipsing binary; its component stars are in a circular orbit with an inclination angle of $\sim$86°.

The primary and secondary components have almost identical semi-amplitudes ($K_1 = 121.2 \pm 0.4$ km s$^{-1}$, $K_2 = 120.5 \pm 0.4$ km s$^{-1}$) and derived properties ($M_* = 0.599$ M$_\odot$, $R_1 = R_2 = 0.619$ R$_\odot$, $T_{\rm eff} = 3800$ K) (Torres & Ribas 2002). From a detailed analysis of existing data including *Hipparcos*, and new spectra of the system, Torres & Ribas (2002) find an inclination of $i = 86\overset{\circ}{.}3$ and derive an age of 370 Myr for the Castor system. These measurements suggest that the primary and secondary stars are separated from each other by about $3.8R_*$. Hatzes (1995) finds that the surfaces of both stars possess low- to mid-latitude spots, predominantly concentrated near 45° latitude.

Very long baseline interferometry (VLBI) studies of the system suggest a large coronal volume, with no evidence of eclipses at radio wavelengths and a coronal size of $2 \times 10^{11}$ cm, closely corresponding to the size of the interbinary distance (Alef, Benz & Güdel 1997). At X-ray wavelengths there is evidence for considerably smaller coronal structures. From *XMM* observations, Güdel et al. (2001) find evidence for three minima indicating X-ray eclipses. These X-ray observations imply that both stars have compact coronal volumes. Güdel et al. (2001) invert their X-ray light curves to construct a coronal model and conclude that the active regions are predominantly within ±50° latitude in a more compact configuration than that indicated by the radio observations alone. Stelzer et al. (2002) conducted coordinated *Chandra* Low Energy Transmission Grating (LETG) and *XMM* observations of YY Gem and analyse a flare found to have a height of $\sim 2 \times 10^9$ cm ($R_* \sim 5$ per cent). Density measurements made from O VII suggest high densities ($\sim 10^{10}$ cm$^{-3}$) and they conclude that the deep eclipses combined with the observed densities and emission measures are consistent with compact coronal volumes in both components. A global fit of *XMM–Newton* EPIC data suggests that loops of the order of $\sim 2 \times 10^9$ cm are consistent with the flare measured at this epoch. They conclude that this flare was associated with one component and there is no evidence of magnetospheric interaction of both component stars.

## 2 OBSERVATIONS

YY Gem was observed over 140 ks, i.e. almost two full rotation cycles ($P_{\rm rot} = 0.814$ d, 70.3 ks) in order to study the structure and dynamics of the component M star X-ray coronae. The *Chandra* observation was split into two pointings, each of which lasted about 70 ks (see Table 1). Over the course of these observations four eclipses are covered, enabling us to identify any potential modulation. The configuration used was the High energy Transmission Grating (HETG) combined with the Advanced CCD Imaging Specotrometer S-array (ACIS-S) to ensure low background and high spectral resolution, both of which are essential for our subsequent analysis.

One of the aims of this study was to conduct a coordinated optical and X-ray study of the eclipsing M dwarf system. We were awarded 141 ks on *Chandra* and three nights on the KPNO 4-m telescope towards this objective. Unfortunately, the coordinated *Chandra* and KPNO campaign was disrupted due to solar flare activity. The X-ray observations were rescheduled from 2006 December to 2007 February, while the optical campaign was conducted as originally planned between 2006 December 12 and 14. In order to have contemporaneous chromospheric monitoring with our X-ray observations, we acquired four moderate-resolution spectra spanning the H$\alpha$ region ($R \sim 0.5$ Å, $6154.29 < \lambda < 6917.5247$ Å) from the Ritter Observatory, USA in 2007 February. The dates and exposure times of these low-resolution spectra are shown in Table 1. The detailed analysis of the earlier KPNO data will be the subject of a separate paper as the spot distribution is significantly altered over a time-scale of one month in active systems such as these (Hussain 2002).

The *Chandra* data were processed using standard CIAO (v.4.1) procedures. The brightest source is YY Gem (Castor C), while Castor A and B are also clearly resolved. Spectra for all three sources were extracted. We focus on YY Gem here. Fluxes and centroids of the extracted Medium Energy Grating (MEG) and High Energy Grating (HEG) spectral line profiles are measured using the SHERPA package.

The resulting ACIS/HETG observations cover three flares: one moderate flare in the first pointing and two strong flares in the second pointing. Flaring and non-flaring states are identified, and the densities and temperatures are measured to probe the location and sizes of the most active regions. Phase-binned spectra are used to measure velocity shifts in the system in both its quiescent and flaring states to analyse the X-ray coronae of the component stars.

The data were corrected for barycentric motions prior to phase folding the data. The ephemeris used is from Torres & Ribas (2002); they define the time of observation, $t_{\rm MJD}$, as a function of the orbital phase, $\phi$, where phases 0 and 0.5 are the phases corresponding to the eclipse of the primary and the secondary star, respectively:

$$t_{\rm MJD} = 49344.612\,327\,87 + 0.814\,288\,2212\phi.$$

**Table 1.** Table of observations.

| ObsID | UT date | MJD | $T_{\rm exp}$ (ks) | Orbital phases |
|---|---|---|---|---|
| Chandra 8504 | 2007 Feb 5 | 54136.8692 | 70.4 | 5885.27:5886.27 |
| Chandra 8509 | 2007 Feb 7 | 54138.4587 | 67.3 | 5887.213:5888.17 |
| Ritter s. 1 | 2007 Feb 8 | 54139.1445 | 2.7 | 5888.02 |
| Ritter s. 2 | 2007 Feb 8 | 54139.1855 | 2.7 | 5888.07 |
| Ritter s. 3 | 2007 Feb 9 | 54140.1354 | 2.7 | 5889.23 |
| Ritter s. 4 | 2007 Feb 9 | 54140.1722 | 2.7 | 5889.28 |

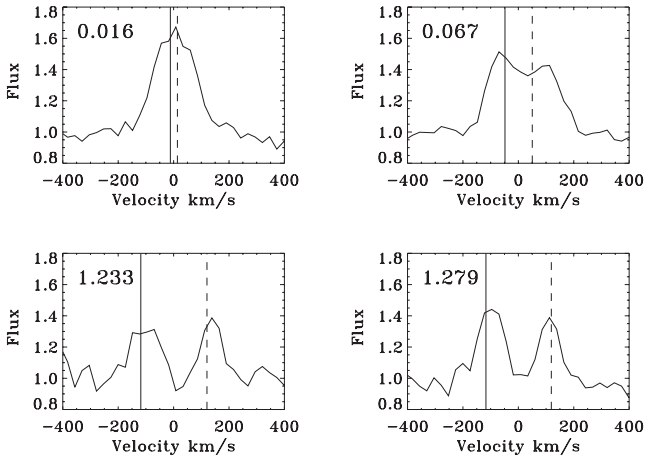


**Figure 1.** H$\alpha$ spectra of YY Gem: these spectra were taken contemporaneously with the *Chandra* data. The corresponding orbital phases ($\phi$ = 5888.0+) are printed above each spectrum and the central velocities of the primary star and secondary star are denoted by a solid line and a dashed vertical line, respectively. The double-peaked line profiles near quadrature indicate that both components of the system are significantly active at this epoch.

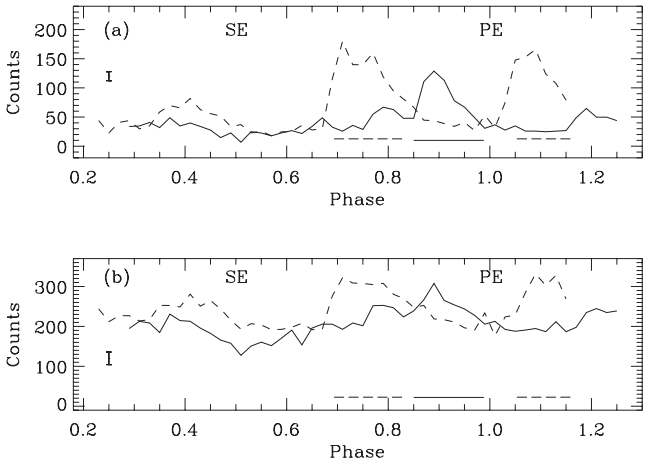


**Figure 2.** Zero-order X-ray light curves with 1400 s (0.02$\phi$) bins. The solid and dashed lines are the first and second pointings, respectively. The start times of the two pointings are separated by 1.95 $P_{\rm rot}$(137 ks). (a) The hard 2–10 keV light curves are used to identify the flaring intervals (marked as horizontal bars, solid and dashed lines represent the first and second pointings, respectively). (b) The 0.3–10 keV light curve with the flaring intervals identified from (a). SE and PE denote the phases corresponding to the secondary and primary eclipses. Typical error bars are shown for each set of light curves.

### 2.1 Chromospheric activity in YY Gem

The H$\alpha$ line profiles from the four contemporaneous optical spectra are all in emission (Fig. 1). The first two spectra were acquired during the rise phase of the last X-ray flare captured during the *Chandra* observations. The mid-times of these H$\alpha$ spectra correspond to phases $\phi$ = 5888.016 and 5888.06, the period before and the period at which the flare started, respectively. There is no obvious sign of H$\alpha$ involvement in this flare. The strength of the profile decreases in the second spectrum at 0.067, but this is expected due to the increased continuum contribution as the primary star emerges from eclipse. The double-peaked profiles near quadrature (Fig. 1, $\phi$ = 1.233 and 1.279) confirm that both components in the system show significant levels of chromospheric activity at the epoch of observations.

## 3 X-RAY LIGHT CURVES

Fig. 2 shows the zero-order phase-folded light curves for both pointings. These two light curves were used to identify flaring states. The 0.3–10 keV light curve is used to identify the 'average' activity level. The quiet, non-flaring state is then defined to be where the count rate is at or below the average count rate. Flaring states are defined to be where the count rate in the 2–10 keV light curve exceeds that in the quiet periods by over 2$\sigma$. This allows the largest flares to be identified, with the first pointing having a lower quiescent count rate (80 per cent) compared to the second, though in agreement within 2$\sigma$. Three flaring intervals are identified in this data set. In the first pointing, the flaring phase is between 0.85 and 0.97. In the second pointing, there are two flaring intervals: 0.69–0.83 and 1.05–1.13.

Fig. 3 shows the light curves extracted from the summed $\pm$1 order HEG and MEG spectra. These were extracted by dividing the phase-folded light curves into 0.02$\phi$ (1.4 ks) bins. Fig. 3(a) shows light curves that were extracted by summing spectra over soft X-ray lines with peak formation temperatures $kT$ between 0.17 and 0.544 keV (see Table 3). This figure demonstrates that integrating only over the soft X-ray lines can eliminate a significant contribution from the flaring continuum. In the first pointing (solid line), there is little involvement in the soft X-ray plasma corresponding to the flare that

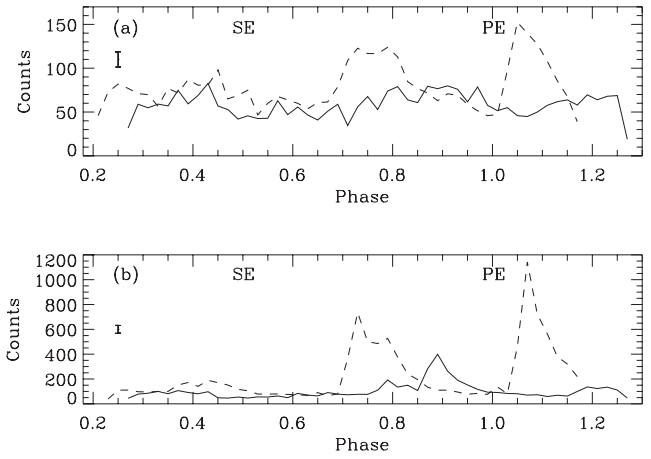


**Figure 3.** X-ray light curves produced by summing up counts over lines in $\pm$1 order HEG and MEG spectra; the bin size used here is 0.02$\phi$ (1400 s). Solid and dashed lines represent the first and second pointings as in Fig. 2. (a) The X-ray light curve formed from lines at soft energies (Mg XI, O VII, O VIII, Ne IX, Ne X, Fe XVII; up to a peak formation temperature of 0.544 keV). (b) The hard X-ray light curve produced by integrating counts over the 1–8.3 Å (1.5–12.4 keV) band. Typical error bars are shown for each set of light curves.

is observed at harder X-rays (near $\phi$ = 0.88). By contrast, there is clear involvement of the soft plasma in both of the flares that are observed in the second pointing (dashed line).

Optical light curves of YY Gem show deep eclipses for both component stars, lasting 0.05$\phi$ from first to fourth contact. Given the system's inclination angle (86.°3) and the equal sizes of the stars, partial eclipses block almost 80 per cent of the eclipsed star's light (Torres & Ribas 2002). As described in Section 1, a previous *XMM–Newton* study of YY Gem found evidence of deep X-ray eclipses (Güdel et al. 2001; Stelzer et al. 2002). The X-ray light curves had 300 s bins ($\Delta\phi$ = 0.004$\phi$) and showed clear minima associated with all the three eclipses (two primary and one secondary eclipse)

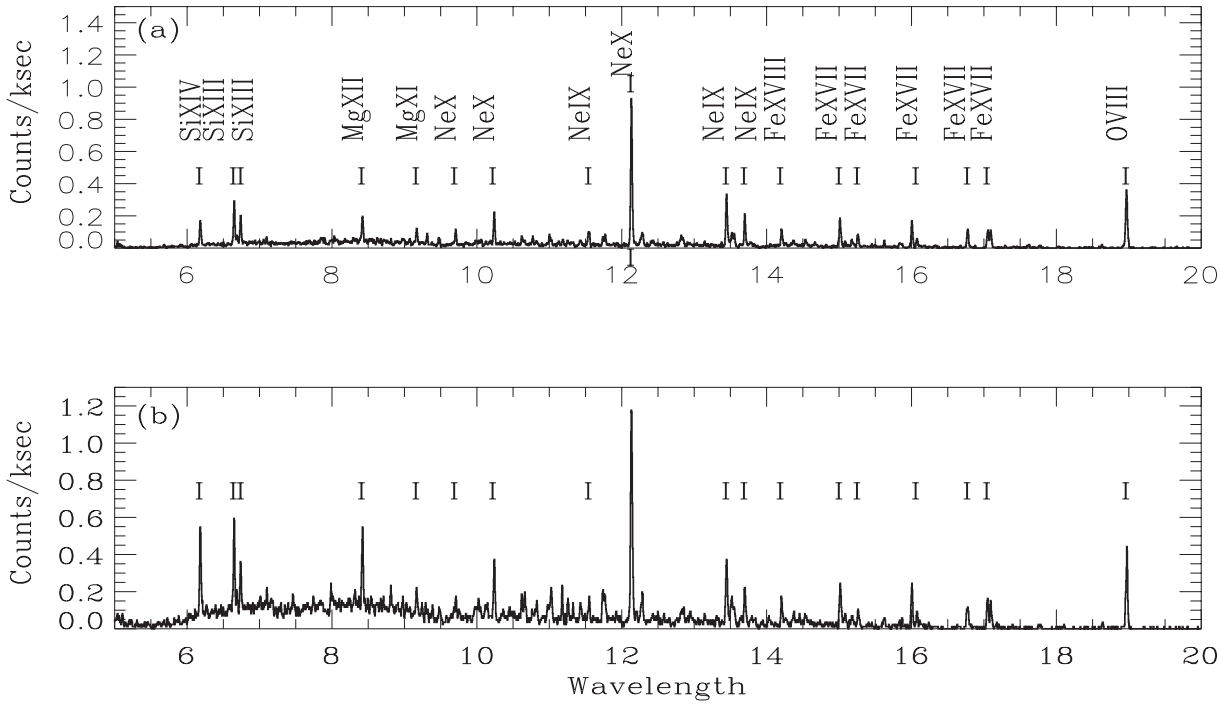


**Figure 4.** (a) The quiet and (b) flaring MEG spectra. ±1 orders have been summed over both sets of observations. There is clearly an enhanced continuum below 10 Å in the flaring spectrum as well as stronger Fe XIX–XXIV lines at 10.66, 10.81, 11.0–11.2 and 11.77 Å.

that were covered in the observation. Stelzer et al. (2002) observe YY Gem with both *XMM–Newton* and *Chandra*/LETG covering one (secondary) eclipse and find evidence of a shallow minimum.

Our observations cover four eclipses; however, the light curves shown in Fig. 2 are binned to 1400 s ($\Delta\phi = 0.02\phi$) and are not very sensitive to the time-scale of the eclipse. We examine X-ray light curves using $0.01\phi$ binning separately and find that even though these light curves are much noisier there is tentative evidence for a minimum at $\phi = 0.5$ (i.e. secondary eclipse) in the first observation. None of the remaining three eclipses show minima even in the $0.01\phi$-binned X-ray light curves, indicating that a significant fraction of the emission is either extended or else concentrated in a compact region preferentially within 40° of only the 'northern' (or upper) poles of the stars. We discuss the X-ray emission models that are consistent with the X-ray light curves and spectra in Section 7.

## 4 SPECTROSCOPIC DIAGNOSTICS: FLARING AND QUIET CORONAL STATES

The quiescent and flaring coronal spectra are shown in Fig. 4, with the strongest lines labelled. These were produced by integrating counts over both ±1 MEG orders over both pointings. We define flaring and non-flaring intervals using the criteria described in Section 3. The flare spectrum clearly shows an enhanced continuum and strengthened Fe XIX, XXIII, XXIV, Si XIII and Si XIV (formed between 0.862 and 1.366 keV). In contrast, the Ne IX line strengths near 13.5 Å appear relatively unchanged in the flaring and quiescent states; this line has a peak formation temperature of 0.343 keV.

### 4.1 Densities

The most easily resolved He-like transitions in this spectral range are the O VII, Si XIII and the Ne IX triplets. Fluxes are measured by fitting Gaussian profiles. While the continuum level varies with wavelength over the full data set, a straight line is a suitable approximation over the small wavelength region in each of these He-like triplets. The O VII line measurements are based on only the −1 order MEG spectra (as there are few counts at this wavelength range in the +1 order); the other diagnostics shown here are based on simultaneous fits to both ±1 MEG order spectra. Strong iron line blends are also accounted for in the Ne IX line fits. Table 2 lists the fluxes measured for the O VII, Ne IX and Si XIII He-like density diagnostics.

To investigate the densities in YY Gem during flares, we integrate over the three prominent flares in our data set to increase the statistics. We then compare these spectra to those produced by integrating over the 'quiet' non-flaring intervals. As the statistics on these fluxes are poor (with 50–60 per cent uncertainties on the flux measurements), a detailed density analysis is difficult. The fluxes from the O VII triplet integrated over the flares are consistent with the low-density limit within $1\sigma$ (Fig. 5).

The intensities of the Si XIII lines at ∼0.862 keV (near 6.65 Å) strengthen during the flares (Fig. 4), but the relative densities remain unchanged and are consistent with the low-density limits. Non-flaring fluxes in particular agree with those measured using YY Gem X-ray spectra taken in 2000 September, i.e. approximately 6.5 years prior to these observations (Stelzer et al. 2002).

## 5 INVESTIGATING X-RAY VELOCITIES

In order to probe the structure of the X-ray coronae in this system during both the flaring and non-flaring states, we analyse velocity shifts in the *Chandra* spectra as a function of orbital phase. Due to the three prominent flares observed over the course of the two pointings, it is not possible to detect rotational modulation of the fluxes. Here we examine the spectra integrated over a range of prominent relatively isolated emission-line profiles for the MEG and HEG spectra separately to generate a higher signal-to-noise ratio composite line profile with greater diagnostic potential than

**Table 2.** Fluxes of density-sensitive diagnostics: resonance, intercombination and forbidden line fluxes are listed here for the two separate pointings and for the spectra in and out of the flare. Only the −1 order had sufficient coverage of the O VII region; for the Ne IX fits, we fitted the +1 and −1 orders simultaneously.

| Wavelength (Å) | Flux ($\times 10^{-4}$) (photons $s^{-1}$ $cm^{-2}$) | Err ($\times 10^{-4}$) | *f*/*i* | Wavelength (Å) | Flux ($\times 10^{-4}$) (photons $s^{-1}$ $cm^{-2}$) | Err ($\times 10^{-4}$) | *f*/*i* |
|---|---|---|---|---|---|---|---|
| Flare | | | | Non-flare | | | |
| O VII (−1) | | | $0.7 \pm 0.6$ | | | | $2.5 \pm 7$ |
| 21.606 | 1.86 | 0.63 | | 21.602 | 1.49 | 0.47 | |
| 21.803 | 1.13 | 0.62 | | 21.797 | 0.29 | 0.77 | |
| 22.103 | 0.76 | 0.50 | | 22.100 | 0.73 | 0.46 | |
| Ne IX | | | $3 \pm 1$ | | | | $4 \pm 1$ |
| 13.447 | 1.65 | 0.27 | | 13.446 | 1.31 | 0.12 | |
| 13.549 | 0.33 | 0.12 | | 13.553 | 0.22 | 0.06 | |
| 13.701 | 1.03 | 0.24 | | 13.699 | 0.95 | 0.11 | |

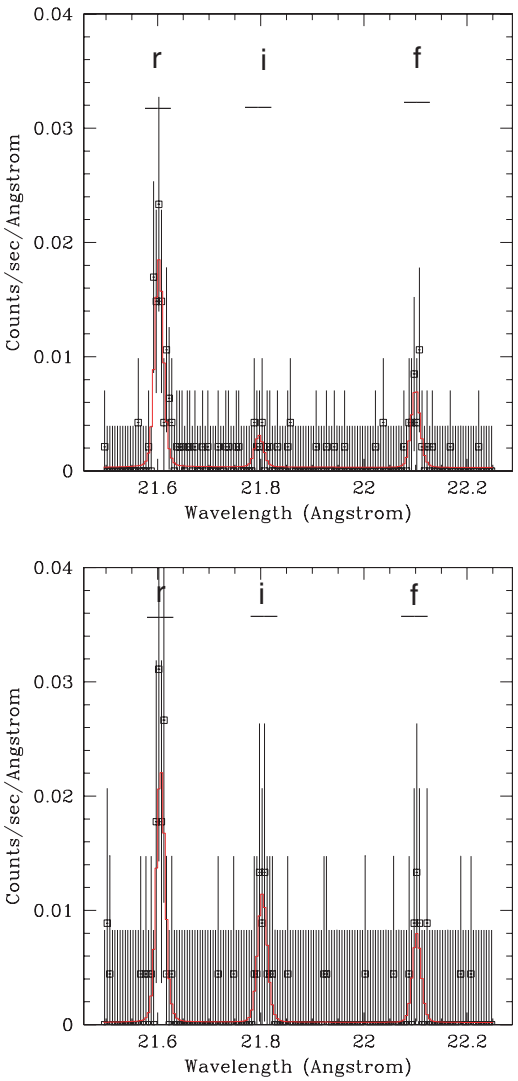


**Figure 5.** O VII density-sensitive diagnostics. Top: non-flaring density diagnostics. Bottom: flaring density diagnostics. The error bars correspond to the $\pm 2\sigma$ uncertainties. The fluxes from the O VII triplet integrated over the flares are consistent with the low-density limit within $1\sigma$.

the individual lines in our data sets. In Section 5.1, we describe how these high signal-to-noise ratio composite profiles are produced. The composite profiles for the full MEG and HEG data sets are presented in Section 5.2; in Section 5.3, we discuss the composite profiles from the non-flaring phases. Section 5.4 investigates the behaviour of the composite profiles generated from lines that are formed at high temperatures.

### 5.1 Composite line profiles: summed spectra

We use an approach first used by Brickhouse et al. (2001) to analyse velocities in the coronae of contact binary systems (also see Hoogerwerf, Brickhouse & Mauche 2004; Huenemoerder et al. 2006). For each pointing, we create spectra integrated over $0.2\phi$ bins (1400 s) in order to obtain sufficient counts for the subsequent analysis; hence five independent spectra can be obtained for each of the pointings.

It is possible to probe dynamics on time-scales that are shorter than $0.2\phi$ by extracting spectra shifted over different intervals. We apply a time shift of $0.04\phi$ between each extracted spectrum, i.e. extracting spectra between phases 0.00 and 0.2, 0.04 and 0.24, 0.08 and 0.28, 0.12 and 0.32, 0.16 and 0.36, 0.20 and 0.40, etc. In this sequence, only the first and last spectra are independent of each other but the extraction over intermediate time bins enables us to investigate the system dynamics in more detail. In this way, about 25 time-resolved spectra are created for each pointing. In each extracted spectrum, well-isolated emission lines are chosen to create composite line profiles with better statistics. The composite line profiles are constructed as described below.

(i) The central wavelengths are measured for the strongest emission lines in the MEG and HEG spectra for each observation, integrating over the entire exposure. This is used to define the zero-velocity position of each line and accounts for any shifts in the relative wavelength scales in the different pointings. We use 24 strong emission lines in the MEG spectra and 10 emission lines in the HEG spectra (Table 3). The centroids of these lines can be measured to a precision of 0.0015 Å or better.

(ii) All of the selected lines in the $0.2\phi$ spectrum are converted into velocity space using the central wavelengths determined in the previous step.

(iii) At each phase, the spectra are interpolated on to the same velocity scale and summed up to create a composite line profile.

(iv) The results are compared for −1 and +1 orders for MEG and HEG spectra separately before summing them up. We treat HEG and MEG separately as the HEG lines have superior spectral resolution but poorer statistics. By examining the HEG and MEG lines separately, we can check the composite line profiles and identify whether any systematic errors were introduced in the centroiding procedure. We find that the velocity shifts shown in the MEG and

**Table 3.** The emission lines used to build the composite line profiles. The columns show the ion used, the peak formation temperature and the central reference wavelength. The final column shows a flag to indicate which composite line profile the line was used in: the MEG (M), HEG (H) or flaring (F) composite profiles. The flaring composite line profiles are produced using lines that form at high temperatures and are discussed further in Section 5.4.

| Ion | log $T$ (K) | log $T$ (keV) | $\lambda_\circ$ (Å) | M/H |
|---|---|---|---|---|
| S XV | 7.2 | 1.366 | 5.039 | MHF |
| Si XIV | 7.39 | 1.366 | 6.183 | MH |
| Si XIII | 7.03 | 0.862 | 6.648 | MHF |
| Si XIII | 7.01 | 0.862 | 6.74 | MHF |
| Mg XII | 7.19 | 0.862 | 8.422 | MHF |
| Mg XI | 6.83 | 0.544 | 9.169 | MH |
| Ne X | 7.01 | 0.544 | 9.481 | MF |
| Ne X | 7 | 0.544 | 9.708 | M |
| Ne X | 6.99 | 0.544 | 10.239 | MH |
| Fe XXIV | 7.19 | 1.719 | 11.18 | F |
| Ne IX | 6.64 | 0.343 | 11.544 | M |
| Ne X | 6.95 | 0.544 | 12.135 | MH |
| Ne IX | 6.61 | 0.343 | 13.447 | MH |
| Ne IX | 6.59 | 0.343 | 13.699 | M |
| Fe XVIII | 6.84 | 0.685 | 14.208 | M |
| Fe XVII | 6.71 | 0.544 | 15.014 | MH |
| Fe XVII | 6.71 | 0.544 | 15.261 | M |
| O VIII | 6.71 | 0.273 | 16.006 | M |
| Fe XVII | 6.71 | 0.432 | 16.78 | M |
| Fe XVII | 6.71 | 0.432 | 17.051 | M |
| Fe XVII | 6.7 | 0.432 | 17.096 | M |
| O VIII | 6.66 | 0.273 | 18.97 | M |
| O VII | 6.35 | 0.172 | 21.602 | M |

HEG composite line profiles are in agreement thus enabling us to ascertain where the dominant X-ray emission is located in the system with a higher degree of confidence.

### 5.2 Composite line profiles: full data set

Figs 6(a)–(d) show the stacked composite MEG and HEG line profiles for the two observations of YY Gem. The higher spectral resolving power and fewer counts in the HEG spectra are apparent. The precision with which the centroids of line profiles can be measured depends on the spectral resolution, the velocity bin size and the peak signal. During the peak counts (i.e. during the flares), these composite line profile centroids can be measured with a precision of approximately 40 and 60 km s$^{-1}$ for the MEG and HEG data sets; more precision is possible in the second MEG exposure due to the increased X-ray emission. In Section 7.1, a series of simulations are used to investigate how the diagnostic power of composite line profiles are affected by an improved spectral resolution and a higher signal. Despite these differences, both the MEG and HEG stacked spectra show consistent velocity variations. By analysing the width, amplitude and variations in velocity space of this composite line profile, it is possible to study the dynamics of the X-ray coronae in the system (e.g. Brickhouse et al. 2001).

In the first observation, ObsID 8504, the peak emission traces the orbital motion of the primary star, though there appears to be a contribution from both component stars (Figs 6a–d). This can be deduced by the broad HEG and MEG profiles leading up to the primary eclipse near phase 0.9. While the peak of the profile is suppressed near the secondary eclipse at $\phi = 0.5$, the amplitude is still relatively high, with peak counts of 100 and 20 in the MEG and HEG composite line profiles, respectively. Near phase 0.9, the light curves show that the flare is near its maximum. At the same phase, the primary star has a central velocity of 70 km s$^{-1}$. Fig. 6 also shows that the peak emission is in the 0–100 km s$^{-1}$ bin, so it may be associated with the primary star. Following the flare at phase 0.9, the emission moves to the $-100$ to 0 km s$^{-1}$ bin also following the movement of the primary star. This may be evidence of the flare originating on the primary star.

The system was more active during the second observation, ObsID 8509, as reflected in the higher counts in the composite line profiles (Figs 6c and d). The MEG and HEG profiles near the start of the observation at phase 0.4 are well centred between both component stars, which may indicate that both components are active. The light curves show that there are two prominent flares during this observation and these dominate the emission in these stacked composite profiles. These flares start near phases 0.70 and 1.05. The X-ray light curves (Fig. 2) suggest that the first flare has two peaks with a second peak near phase 0.80. The velocities of the composite profile follow the primary's orbital velocity between phases 0.7 and 0.8 as does the subsequent decay, which lasts until $\phi = 0.85$. The emission from the second flare near phase 1.05 may come from either star as emission is split between both components, as it is during the subsequent decay, which lasts up to the end of the observation.

### 5.3 Composite line profiles: quiescent phases

The dynamics of the 'quiet' coronae can also be investigated using composite stacked spectra in Figs 7(a)–(d); the quiet coronal level is defined according to the criteria in Section 3. These spectra were extracted excluding the flaring phases that were identified in Section 3: $0.77 < \phi < 0.97$ in ObsID 8504 (the first pointing); and $0.69 < \phi < 0.83$ and $1.05 < \phi < 1.13$ in ObsID 8509 (the second pointing). The excluded phases are marked by horizontal bars in Fig. 2. The composite profiles are produced as described in Section 5.1; by integrating over all well-resolved emission lines using $0.2\phi$ bins at $0.04\phi$ intervals.

In the first observation (ObsID 8504), the quiescent emission is variable over time. The better resolved HEG spectra indicate contributions from both components (Fig. 7b). However, the HEG counts are low so the double-peaked emission near quadrature at phase 0.7 here is not significant, and at the level of the noise. In the second observation, the quiet emission appears to be raised compared to the first observation at all 'quiet' phases, as shown in the X-ray light curve (see Section 3 and Fig. 2). Furthermore, the secondary star contributes more to the quiet emission in the second observation in both the MEG and HEG spectra (e.g. near phase 0.45 – lower plots in Figs 7a–d). Prior to the start of the second flare at $\phi = 1.05$, the emission is broad and subdued compared to that of earlier phases. In the subsequent flare, there appears to be contribution from both component stars. We analyse the high-temperature spectra most likely to be associated with the large flares below.

### 5.4 Composite line profiles: high-temperature diagnostics

Fig. 8 shows the composite line profiles stacked by orbital phase obtained by integrating lines formed at the high-temperature range, i.e. >10 MK. These lines predominantly form in high-temperature plasma associated with energetic flares. Only MEG spectra could be used to generate these profiles as there are insufficient counts in

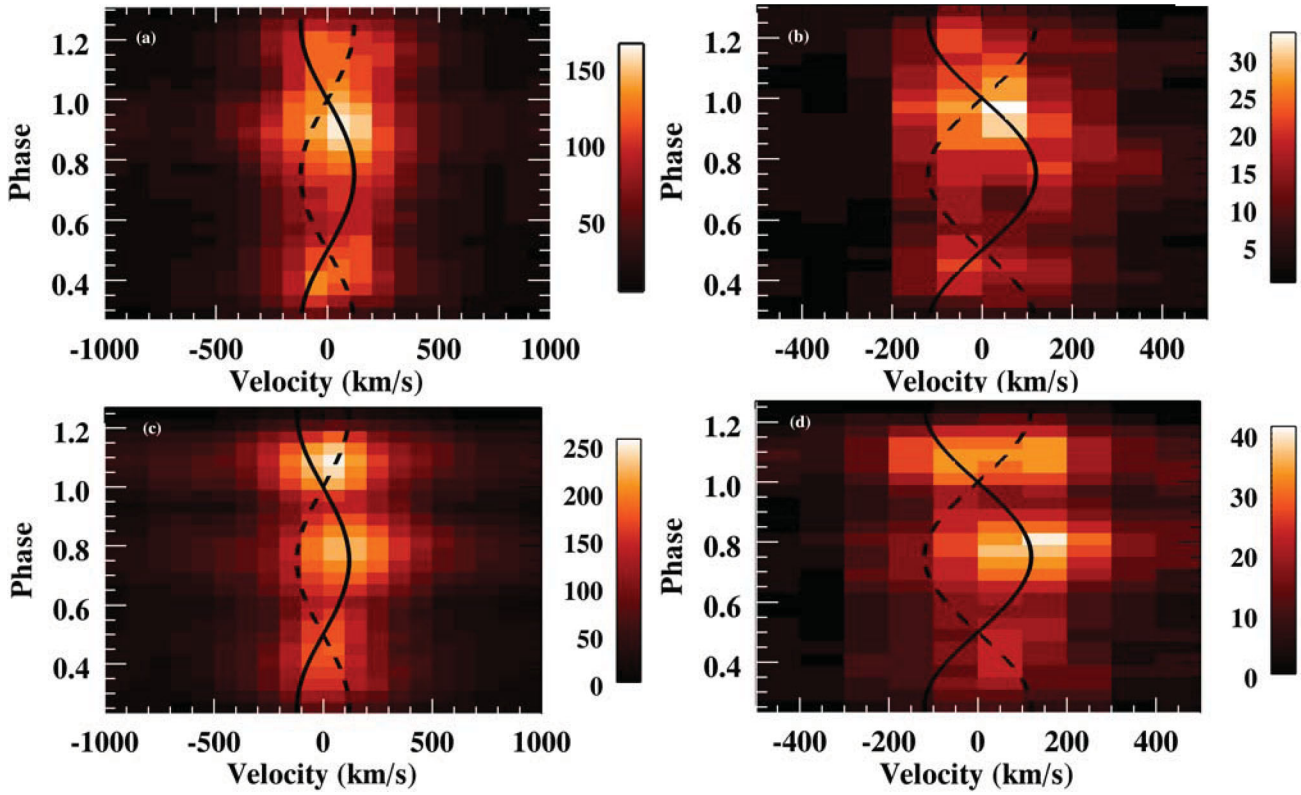


**Figure 6.** Composite line profiles in MEG (left) and HEG (right) ±1 orders for ObsID 8504 (top) and ObsID 8509 (bottom). The colour scales have a 10 and 3 count resolution for MEG and HEG, respectively. The errors can be approximated as counts$^{0.5}$ in order to assess the significance of the velocity shifts with orbital phase. The solid and dashed lines represent the orbital velocities of the primary and secondary components of YY Gem, respectively. The orbital parameters were calculated by Torres & Ribas (2002) using optical spectra. The improved velocity resolution of HEG is reflected by the composite line profile being narrower and therefore a narrower velocity scale.

the HEG lines. The lines used are Si XIV 6.18 Å, Si XIII 6.65 Å, Si XIII 6.74 Å, Mg XII 8.42 Å, Ne X 9.48 Å and Fe XXIV 11.18 Å.

In the first observation the counts peak near phase 0.9, which corresponds with the maximum phase of the large flare in this data set. As this flare occurs near primary eclipse the central velocities of the stars are very close at the time of the flare maximum, so it is difficult to discriminate on which component the flare originates. The peak emission of the hot corona following the flare, however, follows the primary in Fig. 8. The flare loop length measured in Section 6 at the flare maximum is $\sim 0.7 R_*$, which is well within the range of loop lengths found on M stars (Mullan et al. 2006).

The first flare in the second observation, near phase 0.7, also appears to be associated with the primary star. As this occurs near quadrature, the two stellar components are well separated and the peak emission is consistent with the primary. From least-squares Gaussian fitting to the composite line profiles in Fig. 6, we find velocity shifts in the line centroid of $70 \pm 40$ and $60 \pm 70$ km s$^{-1}$, respectively, for the MEG and HEG profiles centred at phase 0.79, which is consistent with the emission being dominated by the primary star; the primary star's velocity at this phase is 115 km s$^{-1}$. This does not however exclude the possibility of a smaller contribution from the secondary star. The second and last flare in the data set (which starts after phase 1.0) is stronger than the previous flares. This flare is particularly interesting as there appears to be significant hot X-ray emission on both components at the time of the flare, which gives evidence for the involvement of both magnetospheres in the development of this flare. This is further supported by centroid measurements of the composite line profiles near flare maximum at phase 1.1. These correspond to velocities of $-27 \pm 40$ km s$^{-1}$ for the MEG profile and $-15 \pm 60$ km s$^{-1}$ for the HEG profile, compared to the primary and secondary star orbital velocities of $-76$ and 76 km s$^{-1}$, respectively.

## 6 FLARE ANALYSIS

In this section, we analyse the flaring light curves and derive loop parameters based on the rise and decay time-scales of the flares. As noted previously, our observations cover three prominent flares; these are called 8504a, 8509a and 8509b in this analysis. The key flaring phases (flare rise, peak and decay) are marked out for the three flares in Fig. 9. We analyse these flares as occurring in single loops. The flaring loop properties can be evaluated by measuring the evolution of the plasma temperatures and emission measures from low-resolution spectra extracted over key phases of the flares.

We first extract low-resolution spectra from the zero order over the quiescent (non-flaring) phases and the rise, peak and decay phases of each of the flares. We fit one-temperature (1-T) and two-temperature (2-T) models to these spectra and find that the low-temperature component in the quiescent phases is $kT = 0.69 \pm 0.01$ keV. Unfortunately, with either 1-T or 2-T modelling we find that the temperatures cannot be constrained well enough to extract a trend useful for the analysis of the decay as in Reale et al. (1997). We therefore obtain information from the analysis of the rise and peak phases according to Reale (2007). In Reale (2007), flares are modelled as being triggered from a heating pulse, the duration of which can affect the delay between the maximum temperature and

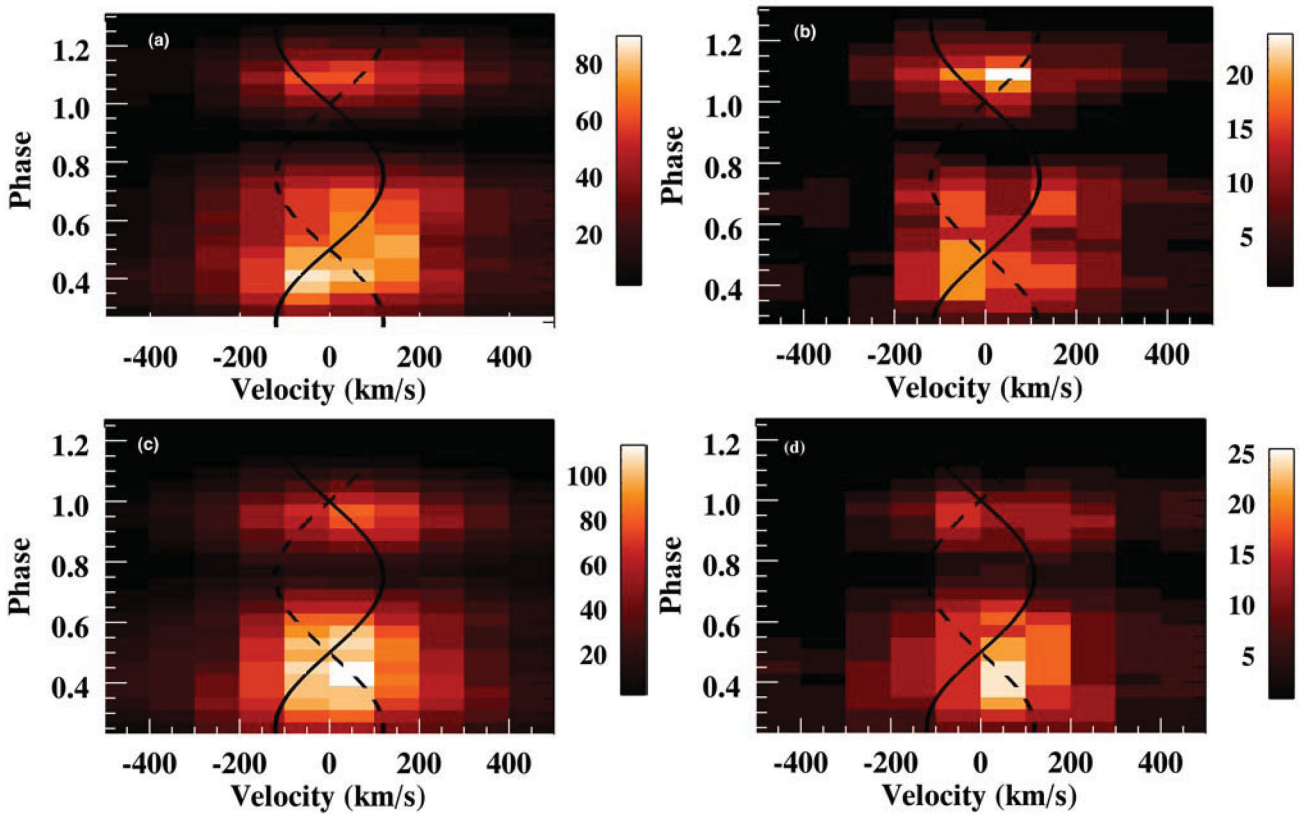


**Figure 7.** Out of flare 'quiescent' emission on YY Gem: composite line profiles from MEG ±1 order spectra (left-hand column) and HEG ±1 order spectra (right-hand column) for ObsID 8504 (top row) and ObsID 8509 (bottom row). The colour scale intervals are every 5 and 3 counts for MEG and HEG, respectively. Solid and dashed lines are the same as in Fig. 6.

maximum density as the flare evolves. They use these hydrodynamic models to derive diagnostic formulae as a function of observable quantities related to the rise phase and maximum phase of the flare. The emission measure values and the peak temperatures are taken from 1-T modelling of the spectra. The loop parameters derived here can be compared to those derived for other stellar flares in table 1 of Reale (2007).

Table 4 shows the measured and calculated parameters. Here, $\tau_{\rm rise}$ is the rise time-scale; $t(T_{\rm max} - n_{\rm max})$ is the delay time between the maximum temperature and density maximum[1]; $T_{\rm obs}$ is the measured temperature at the flare peak; $T_0$, the maximum loop temperature, is calculated using equation (1) (see equation A.1 in Reale 2007); $L_0$ is the loop half-length; $\tau_{\rm decay}$ is the e-folding time-scale of the flare decay; $L_1$ provides an upper limit to the size of the loop length derived from the flare decay time-scale; $n_{\rm M}$ is the maximum density at the loop apex; $r$ is the loop cross-section radius; and $r/L_0$ is the aspect ratio. All the values we calculate for the aspect ratios of these flares are consistent with those expected for a single loop as discussed in Section 7.2. A brief description of how these quantities are calculated is provided below but readers should refer to Reale (2007) for the full derivations.

The maximum loop temperature $T_0$ is

$$T_0 = \xi T_{\rm obs}^{\eta}. \quad (1)$$

Here, $T_{\rm obs}$ is the measured temperature at the flare peak, and $\eta$ and $\xi$ are specific to the instrument used. For *Chandra*/ACIS, $\eta$ and $\xi$ are 1.20 and 0.068, respectively (Reale 2007, table A1). The loop half-length is derived from the ratio of the maximum temperature and the temperature at density maximum (Reale 2007, equations 11 and 12):

$$L_0 \approx 3\psi^2 T_{0,7}^{1/2} t_{\rm M,3}, \quad (2)$$

where $L_0$ is the loop half-length (in $10^9$ cm), $t_{\rm M}$ is the time corresponding to density maximum in ks and $T_0$ is the loop maximum temperature (in units of $10^7$ K). $\psi$ is the ratio of the maximum temperature to the temperature at density maximum:

$$\psi = \frac{T_0}{T_{\rm M}} = \exp\left(\frac{\Delta\tau_{0-{\rm M}}}{1.2 t_{\rm M}}\right), \quad (3)$$

where $T_{\rm M}$ is the temperature at the time of the density maximum and $\tau_{0-{\rm M}}$ is the time between flare maximum and the time at which the density maximum occurs. The associated uncertainty is estimated assuming that the uncertainty on the $t_{\rm M}$ is about half of the time interval of the flare peak.

The e-folding decay time, $\tau_{\rm decay}$, is used to estimate an upper limit to the loop length ($L_1$) independently. For this calculation we assume the minimum possible value for the heating factor, $F(\zeta) \approx 1.9$.

Densities can also be determined for the loop apex in each flare, with $n_{\rm M}$, the maximum density at the loop apex (in units of $10^{10}$ cm$^{-3}$; Reale 2007). The volume can be estimated from the emission measures measured from 1-T fitting and thus the area and radius of the loop cross-section. This is useful to estimate the ratio between the loop length and radius to evaluate whether or not this would realistically correspond to a single loop. Aspect ratios ($r/L_0$)

[1] The time of the light curve maximum is used as a proxy of the time of the emission measure, and therefore of the density maximum (Reale 2007).

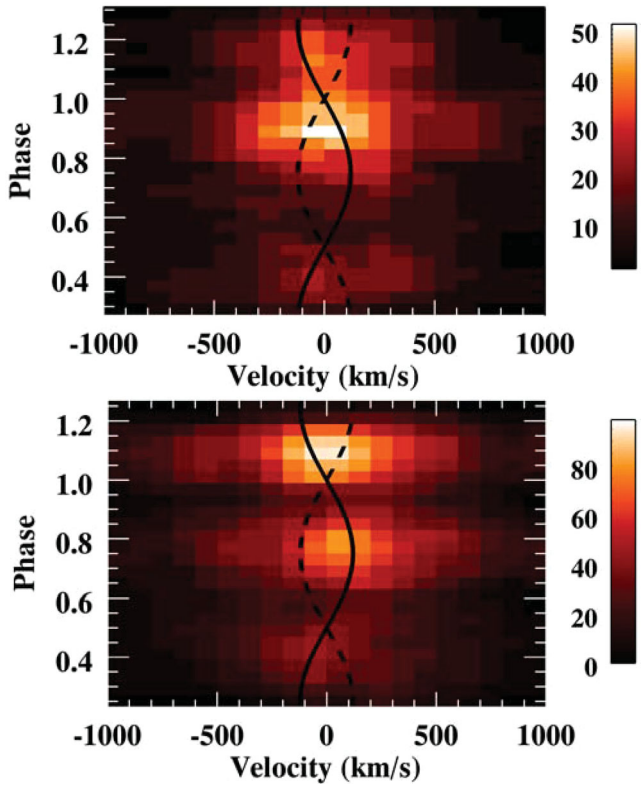


**Figure 8.** High-temperature >10 MK MEG emission in YY Gem for ObsID 8504 (top) and ObsID 8509 (bottom). The colour scale intervals are every 5 counts. The errors can be approximated as counts$^{0.5}$ in order to assess the significance of the velocity shifts with orbital phase. The dashed and solid lines are the same as in Fig. 6.

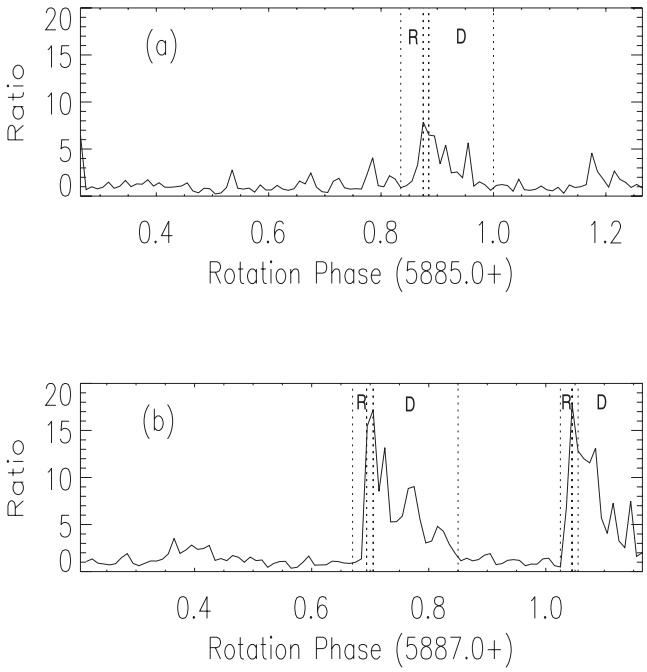


**Figure 9.** Hardness ratio used to help identify flaring intervals; this is the ratio between the 2–10 and 0.3–0.7 keV light curves. The dotted lines represent the rise (R), maximum and decay (D) phases for the prominent flares in the two pointings: (a) ObsID 8504 and (b) ObsID 8509.

are found to be under 0.15 for all three flares observed on YY Gem; these are therefore consistent with flares occurring in typical single coronal loops (Golub et al. 1980; Peres et al. 1987).

## 7 DISCUSSION AND SUMMARY

At this epoch, both components of YY Gem are clearly active as evidenced by the lack of strong eclipses in the X-ray light curves and double-peaked emission-line profiles in the H$\alpha$ line profiles obtained at the same time as the X-ray observations. The previous *XMM–Newton* study by Güdel et al. (2001) showed two deep primary and one secondary eclipse in the X-ray light curves. We find tentative evidence for a decrease in the X-ray emission corresponding to the primary eclipse in the first X-ray light curve of the first observation but not in the other three eclipses (one primary and two secondary) covered in these observations. This implies that the distribution of the X-ray-emitting regions is different, either with activity at the poles and/or extended emitting regions. We have produced composite line profiles, which have been used to great effect in the investigation of close binary stars in the past. In YY Gem the analysis is complicated by the comparatively smaller orbital velocities of the components ($K_1 = 120\,\mathrm{km\,s^{-1}}$), the equal activity level of both components and the three large flares. As both the instrumental resolution and the signal-to-noise ratio are necessarily limited in the data, it is difficult to disentangle how the X-ray-emitting volume is distributed in this system. We investigate the minimum data requirements to probe stellar coronae and discriminate between different types of X-ray distributions using simulations of X-ray coronae and convolving these with different instrument resolutions and noise levels.

### 7.1 Probing stellar coronae: X-ray spectra requirements

In this section, we seek to quantify the instrumental resolution and signal-to-noise ratio needed to effectively probe the X-ray coronal distribution in active cool star binary systems such as YY Gem. The composite line profiles presented in Section 5 have instrumental profiles with a full width at half-maximum (FWHM) of 400 km s$^{-1}$ for the MEG composite line profiles and 300 km s$^{-1}$ for the HEG composite line profiles. The best resolved individual line profile in our data set is the HEG 15.01 Å Fe XVII line diagnostic with a FWHM of 200 km s$^{-1}$.

We generate very simple models of X-ray coronae, simply exploring the effect of a non-time-variable corona with stable 'quiescent' X-ray active regions. The compact models assume an X-ray corona with a height of about $0.05R_*$, while the extended coronal model has a maximum height of $1R_*$ in these initial models. We assume a 2-T X-ray corona in these simple simulations, with the only modulation caused by rotational modulation of active regions. The contribution from the active regions to the computed X-ray profiles depends on the visibility of the active region, the area of these regions projected along the line of sight at each orbital phase using an adapted version of the Doppler imaging code, DOTS (e.g. Dunstone et al. 2008). The X-ray profiles from each pixel in the coronal volume can be modelled as a Gaussian profile.

Examples of our simulated spectra for four different X-ray coronal models are shown in Fig. 10. The left-hand column shows the original simulations; from top to bottom, there are three compact coronal models: (a) a simple polar active region on only one star; (b) both stars host active polar regions but the primary also hosts an additional low-latitude active region; and (c) even distribution of active regions in the entire coronal volume. The fourth model

**Table 4.** Flare diagnostics.

| Flare ID | $\tau_{\rm rise}$ (ks) | $t(T_{\rm max} - n_{\rm max})$ $\Delta t_{0-{\rm M}}$ (ks) | $T_{\rm obs}$ ($\times 10^7$ K) | $T_0$ ($\times 10^7$ K) | $L_0$ ($\times 10^9$ cm) | $\tau_{\rm decay}$ (ks) | $L_1$ ($\times 10^9$ cm) | $n_{\rm M}$ ($\times 10^{10}$ cm$^{-3}$) | $r$ ($\times 10^9$ cm) | $r/L_0$ |
|---|---|---|---|---|---|---|---|---|---|---|
| 8504a | $2.8 \pm 0.5$ | 0.7 | $2.3 \pm 0.3$ | $4.6 \pm 0.7$ | $28 \pm 10$ | 5.8 | $\leq 53$ | $6 \pm 4$ | 4 | 0.15 |
| 8509a | $4.2 \pm 0.5$ | 2.1 | $3.1 \pm 0.6$ | $6.7 \pm 1.6$ | $75 \pm 15$ | 7.0 | $\leq 78$ | $3 \pm 2$ | 6 | 0.09 |
| 8509b | $3.5 \pm 0.5$ | 1.4 | $3.9 \pm 0.7$ | $8.8 \pm 1.9$ | $61 \pm 15$ | 6.1 | $\leq 78$ | $8 \pm 5$ | 4 | 0.06 |

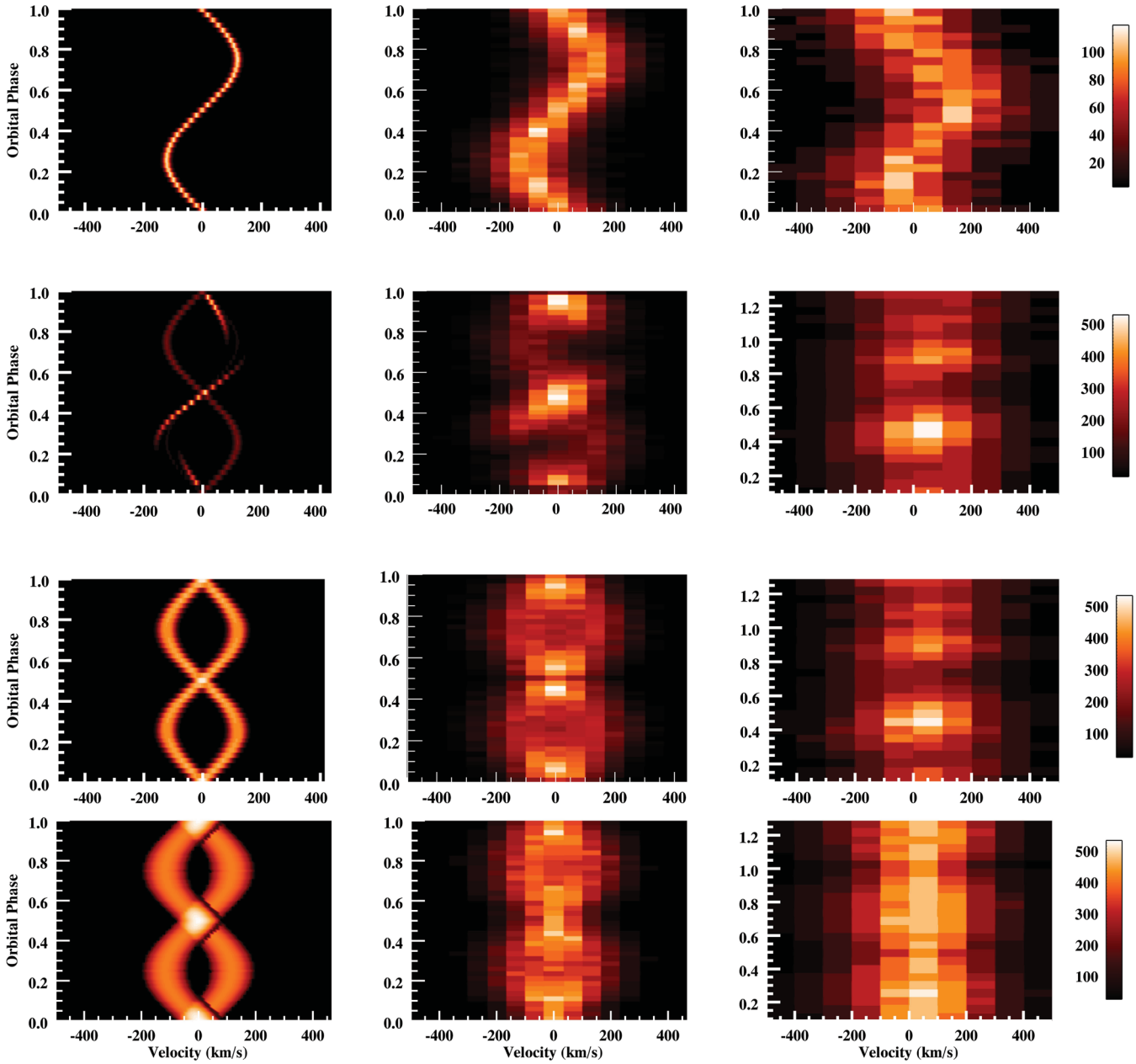


**Figure 10.** This plot shows dynamic simulated spectra. Top to bottom: four different coronal models were used. Top row: one compact X-ray-emitting polar region on the primary star only; second row: the primary star has two X-ray active regions at high and low latitudes and the secondary has a polar X-ray-emitting region; third row: both stars have an evenly distributed compact corona (<5 per cent of $R_*$); bottom row: the corona is evenly distributed and extends out beyond $1R_*$. The left-hand column shows the original simulated spectra; the middle column shows the simulations convolved with a FWHM of 200 km s$^{-1}$ instrumental profile and spectra with peak counts of 300. The right-hand column shows the simulations convolved with a FWHM of 400 km s$^{-1}$ instrumental profile and binned in phase over $0.2\phi$, these spectra have peak counts of 500 (a factor of 5 more than our quiescent spectra – cf. Fig. 8).

is of an extended X-ray corona with even emission throughout a $1R_*$ coronal volume. Left to right: the first column shows the original profiles from the simulations, the middle column shows these profiles binned into $0.025\phi$ bins and convolved with instrument profile widths of 200 km s$^{-1}$ (corresponding to the best resolution attainable in a single line, Fe XVII 15.01 Å, with HEG) and with added noise (peak counts of 300). The last column shows the spectra binned over $0.2\phi$, as shown in Section 5 with noise added (peak counts of 500).

As noted above, this figure can also be used to explore signal-to-noise ratio limitations. The throughput in the 200 km s$^{-1}$ convolved spectra corresponds to an improvement in throughput of over 65 times compared to the strongest individual MEG line profile (Ne X at 12.1 Å) and an instrumental resolution equivalent to the best resolved HEG line profile in our data set. With these simulations, it is possible to distinguish between different active region distributions with discrimination easily possible between the different compact models. While compact model (b), which has two active regions on the primary, cannot be precisely mapped it is possible to see that both components are active with more than one active region involved. The discrimination between compact and extended models is clearly more challenging with the loss of spectral resolution.

The third column shows the simulations convolved with an instrumental profile with a FWHM of 400 km s$^{-1}$ and binned up in $0.2\phi$ segments. These have been computed in a similar manner to the composite line profiles in Fig. 7 but with a signal-to-noise ratio increased by a factor of 5 with respect to the quiescent composite line profiles (peak counts of 500). What these simulations show is how much information is necessarily lost by binning up by $0.2\phi$. While it is still possible to distinguish between a system with only one active star and two active stars, if there is only one dominant active region this will show clearly even in these binned spectra. If both stars have similar levels of activity, then the emission predominantly remains confined to the central velocity bins. The velocity evolution seen in the high-temperature composite line profiles (Fig. 8) does therefore probably trace the movement of the primary star.

### 7.2 X-ray coronae in YY Gem

We detect three large flares in a total exposure time of 1.6 d. Including previous *Chandra* and *XMM–Newton* observations of the system, this adds up to a total exposure of 3.4 d (1.03 d: Güdel et al. 2001; 0.78 d: Stelzer et al. 2002; 1.6 d: this paper). With nine flares detected in these observations, this leads to an average flaring rate of one every 9 h. However, the system's flaring frequency may not be consistent over a period of years and there may be long-term changes in its activity state that are not well characterized. Previous observations of YY Gem report X-ray luminosities ranging $2–8 \times 10^{29}$ erg s$^{-1}$ in the soft X-ray band (Stelzer et al. 2002). We find X-ray luminosities in the 0.2–2.0 keV ACIS band of $3–3.5 \times 10^{29}$ erg s$^{-1}$ in the 'quiet' data (i.e. excluding the large flares). We measure X-ray luminosities during the flare maximum of 5, 7.5 and $13 \times 10^{29}$ erg s$^{-1}$ for the three flares in our data set. These are consistent with the range of X-ray luminosities reported during the flares of active main-sequence stars (e.g. Pandey & Singh 2008).

Studies looking at flaring properties of main-sequence stars have uncovered trends with spectral type. Mullan et al. (2006) analyse over 100 flares from 33 active stars, including single and binary systems, covering a range of spectral types. They find that the flaring loop sizes found in M stars can be significantly larger ($L \leq 1.5R_*$; $L \leq 45 \times 10^9$ cm) than those found in G and K star systems (typically $<0.5R_*$). Radio observations can also be used to characterize the sizes of stellar magnetospheres, through the detection of gyrosynchrotron radiation emitted by relativistic electrons in magnetic loops. Benz, Conway & Güdel (1998) also find evidence of radio emission of the dM5.5e binary with lengths between $2.2R_*$ and $4R_*$. Even larger flaring loops are found from a detailed analysis of over 260 flares in T Tauri stars in the Orion nebula cluster, with loop lengths above $10^{12}$ cm (Getman et al. 2008).

Previous X-ray observations of YY Gem were interpreted as a mixture of compact ($0.05R_*$) and longer loops ($>0.75R_*$) (Güdel et al. 2001; Stelzer et al. 2002). By measuring the thermal evolution of each flare during the epochs of rise time, maximum temperature and maximum density epochs, we find flare loop lengths under the hypothesis of single loop flares. Although we cannot exclude that flares occurred in multiloop flaring systems, the hypothesis of single loop flares leads to a consistent scenario with loops that are within the range of those measured for M stars. Two of the flares had longer loops than previously measured for YY Gem: the flare loop lengths are $0.7R_*$, $1.8R_*$ and $1.5R_*$ for flares 8504a, 8509a and 8509b, respectively. The flares with the longest loop lengths were observed when the system was in a higher state of activity. Given a separation of $3.8R_*$ between the component stars (Brancewicz & Dworak 1980), the flare loops are of the same size as half the interbinary separation.

The coronal densities measured in YY Gem in previous studies support a coronal extension of $10^{10}$ cm, or close to $0.3R_*$ (Ness et al. 2004). There is also strong evidence that the magnetospheres of cool stars such as YY Gem extend to much larger radii. Radio observations indicate that YY Gem supports structures extending to greater than $1R_*$. Time series of Balmer line spectra show fast moving transients in absorption, indicating the presence of cool material subtended at distances of up to $\sim 3R_*$ and co-rotating with the star, e.g. in the K0V, AB Dor and K3V, BO Mic (Dunstone et al. 2006; Hussain et al. 2007). *Hubble Space Telescope*/ STIS observations of the binary system, V471 Tau (DA + K2V), also reveal a 0.25 MK atmosphere extending out to the Keplerian co-rotation radius of the K2 star (Walter 2004). Surface magnetic field maps of YY Gem would enable us to model the binary magnetospheric interaction of the system in more detail (cf. the pre-main-sequence binary star, HD 155555; Dunstone et al. 2008).

Recently, magnetospheric interaction between stars in a close binary system has been found to occur in the T Tauri binary system, DQ Tau (Salter et al. 2010; Getman et al. 2011). The high eccentricity of DQ Tau's orbit leads to a periodic flaring in millimetre (mm) and X-ray wavelengths. These flares occur when the system nears periastron (with an interbinary distance of $8R_*$); the mm emission region is located halfway between the binary stars with a height of $3.7–6.8R_*$. Similar effects are noted for the T Tauri binary, V773 Tau A, which shows radio flares near periastron (Massi et al. 2006; Torres et al. 2012). Adams et al. (2011) produce models explaining how interactions from binary magnetic fields can change the magnetic energy stored in the system, an effect that will be more pronounced in eccentric binary orbits such as in DQ Tau and V337 Tau A. The magnetic energy stored in close binary systems with circular orbits must also be enhanced and dissipated due to interactions between the two stellar coronae.

Due to the presence of the large X-ray flares, it was not possible to measure rotational modulation that might originate in the softer X-ray corona as has been possible with AB Dor (Hussain et al. 2007). Instead we examine the velocity shifts in the emission-line spectra by constructing composite line profiles from the strongest, most isolated, emission lines in the data. With the current resolution, it remains difficult to establish whether YY Gem has a compact corona

or whether there is significant extended emission in the system through these spectral line profiles alone. What is clear is that both components are similarly active during these observations, or as confirmed by simulations, a clear trend would be seen following the X-ray active star even with the resolution and signal-to-noise ratio constraints of our data.

With the composite line profiles, we find that the flaring emission on YY Gem predominantly traces the movement of the primary star during the flares observed in both data sets. We also acquired a time series of optical high-resolution spectra that can be used to map spots in the system. Given the challenges with coordinating the X-ray and optical observations, there was a delay by several months between the optical and X-ray observations; the spot activity likely evolves significantly over a period of two months (Hussain 2002). However, it would be instructive to see if the primary star is indeed more active than the secondary, as the flaring data set appears to suggest.

## ACKNOWLEDGMENTS

The authors would like to thank the referee, John Pye, for his careful reading of the manuscript and helpful comments. This research utilized spectra obtained in service observing mode by Nancy D. Morrison, Erica N. Hesselbach and Gregory B. Thompson at Ritter Observatory with support from the NSF-PREST programme under grant no. AST-0440784. FR acknowledges support from Agenzia Spaziale Italiana (ASI), ASI-INAF Contract I/009/10/0. Support for this work was provided by the National Aeronautics and Space Administration through Chandra Award Number GO6-7012X issued by the Chandra X-ray Observatory Center, which is operated by the Smithsonian Astrophysical Observatory for and on behalf of the National Aeronautics Space Administration under contract NAS8-03060. This research has made use of software provided by the Chandra X-ray Center (CXC) in the application packages CIAO and SHERPA.

## REFERENCES

Adams F. C., Cai M. J., Galli D., Lizano S., Shu F. H., 2011, ApJ, 743, 175
Alef W., Benz A. O., Güdel M., 1997, A&A, 317, 707
Benz A. O., Conway J., Güdel M., 1998, A&A, 331, 596
Brancewicz H. K., Dworak T. Z., 1980, Acta Astron., 30, 501
Brickhouse N. S., Dupree A. K., Young P. R., 2001, ApJ, 562, 75
Butler C. J., Doyle J. G., Budding E., 1996, in Pallavicini R., Dupree A. K., eds, ASP Conf. Ser. Vol. 109, Cool Stars, Stellar Systems, and the Sun. Astron. Soc. Pac., San Francisco, p. 589
Canizares C. R. et al., 2005, PASP, 117, 1144
Doyle J. G., Butler C. J., 1985, Nat, 313, 378
Dunstone N. J., Barnes J. R., Cameron A. C., Jardine M., 2006, MNRAS, 365, 530
Dunstone N. J., Hussain G. A. J., Collier Cameron A., Marsden S. C., Jardine M., Stempels H. C., Ramirez Velez J. C., Donati J.-F., 2008, MNRAS, 387, 481
Favata F., Micela G., Reale F., Sciortino S., Schmitt J. H. M. M., 2000, A&A, 362, 628
Getman K. V., Feigelson E. D., Broos P. S., Micela G., Garmire G. P., 2008, ApJ, 688, 418
Getman K. V., Broos P. S., Salter D. M., Garmire G. P., Hogerheijde M. R., 2011, ApJ, 730, 6
Golub L., Maxson C., Rosner R., Vaiana G. S., Serio S., 1980, ApJ, 238, 343
Golub L., Harnden F. R., Maxson C. W., 1983, ApJ, 271, 264
Güdel M., Audard M., Magee H., Franciosini E., Grosso N., Cordova F. A., Pallavicini R., Mewe R., 2001, A&A, 365, 344
Hatzes A. P., 1995, in Strassmeier K. G., ed., Proc. IAU Symp. 176, Poster Proceedings. Universitaet Wien, Vienna, p. 90
Hoogerwerf R., Brickhouse N. S., Mauche C. W., 2004, ApJ, 610, 411
Huenemoerder D. P., Testa P., Buzasi D. L., 2006, ApJ, 650, 1119
Hussain G. A. J., 2002, Astron. Nachr., 323, 349
Hussain G. A. J. et al., 2007, MNRAS, 377, 1488
Kron G. E., 1952, ApJ, 115, 301
Massi M., Forbrich J., Menten K. M., Torricelli-Ciamponi G., Neidhfer J., Leurini S., Bertoldi F., 2006, A&A, 453, 959
Mullan D. J., Mathioudakis M., Bloomfield D. S., Christian D. J., 2006, ApJS, 164, 173
Ness J.-U., Güdel M., Schmitt J. H. M. M., Audard M., Telleschi A., 2004, A&A, 427, 667
Pandey J. C., Singh K. P., 2008, MNRAS, 387, 1627
Peres G., Reale F., Serio S., Pallavicini R., 1987, ApJ, 312, 895
Reale F., 2007, A&A, 471, 271
Reale F., Betta R., Peres G., Serio S., McTiernan J., 1997, A&A, 325, 782
Salter D. M., Kóspál Á., Getman K. V., Hogerheijde M. R., van Kempen T. A., Carpenter J. M., Blake G. A., Wilner D., 2010, A&A, 521, A32
Sanz-Forcada J., Brickhouse N. S., Dupree A. K., 2003, ApJS, 145, 147
Stelzer B. et al., 2002, A&A, 392, 585
Torres G., Ribas I., 2002, ApJ, 567, 1140
Torres R. M., Loinard L., Mioduszewski A. J., Boden A. F., Franco-Hernandez R., Vlemmings W. H. T., Rodriguez L. R., 2012, ApJ, 747, 18
Walter F. M., 2004, Astron. Nachr., 325, 241

This paper has been typeset from a TEX/LATEX file prepared by the author.